

ARTICLE OPEN



CrRhAs: a member of a large family of metallic kagome antiferromagnets

Y. N. Huang¹, Harald O. Jeschke² and Igor I. Mazin^{3,4}✉

Kagome lattice materials are an important platform for highly frustrated magnetism as well as for a plethora of phenomena resulting from flat bands, Dirac cones and van Hove singularities in their electronic structures. We study the little known metallic magnet CrRhAs, which belongs to a vast family of materials that includes 3d, 4f, and 5f magnetic elements, as well as numerous nonmagnetic metals and insulators. Using noncollinear spin density functional calculations (mostly spin spirals), we extract a model magnetic Hamiltonian for CrRhAs. While it is dominated by an antiferromagnetic second nearest neighbor coupling in the kagome plane, the metallic nature of the compound leads to numerous nonzero longer range couplings and to important ring exchange terms. We analyze this Hamiltonian and find unusual ground states which are dominated by nearly isolated antiferromagnetic triangles that adopt 120° order either with positive or with negative vector chirality. We discuss the connection to the few known experimental facts about CrRhAs. Finally, we give a brief survey of other interesting magnetic members of this family of kagome compounds.

npj Quantum Materials (2023)8:32; <https://doi.org/10.1038/s41535-023-00562-x>

INTRODUCTION

Due to strong geometric frustration, antiferromagnetism on a kagome lattice is expected to yield complex properties such as classical or quantum spin liquids^{1–4}. A good example with well-localized spin-1/2 copper magnetic moments forming a kagome lattice is herbertsmithite (ZnCu₃(OH)₆Cl₂) which has been drawing a lot of interest since it was first synthesized in 2005⁵. It has long been discussed as a quantum spin liquid candidate⁶ but some kind of structural disorder plays a significant role⁷. Other examples of kagome antiferromagnets which are proximate to or actually realize quantum spin liquids are kapellasite (ZnCu₃(OH)₆Cl₂)^{8,9}, Y-kapellasite (Y₃Cu₉(OH)₁₉Cl₈)^{10,11}, and Zn-barlowite (ZnCu₃(OH)₆FBr)^{12,13}.

Deviations from this “canonical” model have also been attracting a lot of attention lately. One line of inquiry has been along the search for nontrivial magnetic properties in kagome models with more complex interactions. Some examples include ideal kagome with reduced symmetry^{11,14}, breathing kagome forming magnetic trimers^{15–18} (which can host electrons¹⁷ or spin-waves¹⁹ with flat dispersion due to trimerization, as well as semimetals, including Weyl^{20,21}). Yet another direction is introducing anisotropic interactions (like Dzyaloshinskii-Moriya) generating non-coplanar magnetic patterns with non-zero scalar chirality and topological transport^{22,23}, or combining spin-ice Ising terms with twisted kagome geometry²⁴. Of course, these are only a few examples from a potentially long list.

Interestingly, good metals with kagome and kagome-like geometries have only relatively recently been studied intensively. A typical example is the intermetallic T_mX_n kagome series ($T = \text{Mn, Fe, Co}$; $X = \text{Sn, Ge}$; $m:n = 3:1, 3:2, 1:1$) with different kagome plane stackings²⁵. Much effort has been put into studying their topological properties (Dirac fermions and flat bands)^{25–27}. Related kagome metals, such as YMn₆Sn₆, exhibit a nontrivial topological Hall effect^{28–30}, while another kagome metal family, AV₃Sb₅

(A=K,Na,Cs), demonstrates a series of intriguing orders, including superconductivity^{31–34}. Importantly, kagome planes in these systems are not magnetically frustrated, but they retain interesting electronic properties due to the special features of the kagome dispersion: Dirac points, van Hove singularities, and flat bands. Kagome metals with antiferromagnetic frustration have been little studied so far^{35,36}.

Ideal kagome lattices are not uncommon, but relatively rare. An important point in this regard is that most unique properties of kagome magnets do not, actually, require an ideal kagome geometry, but rather an ideal kagome connectivity. In this respect, there is no difference at the nearest neighbor level between a perfect kagome lattice and the one twisted by triangle rotations, as shown in Fig. 1. In this paper, we discuss a large family of compounds with the chemical formula XYZ and space group $P\bar{6}2m$ (no. 189). Typically, they include two metal layers, X and Y with ligands Z integrated into the two layers at a ratio 1:2. Thus, the structure can be understood as a stacking of X₃Z at $z = 0.5$ and of Y₃Z₂ at $z = 0$. Due to two 6-fold rotoinversion axes, the metal planes can be described as twisted kagome, where ligands sit in high-symmetry positions inside the metal planes. One metal sublattice, as discussed below, is only moderately deformed from the ideal kagome, while the other, incorporating two ligand atoms per unit cell, has metals combined into trimers. The former subsystem is often magnetic, the latter usually not.

The elemental base for this crystallographic family, known by its prototype ZrNiAl, where X = Zr, Y = Al, and Z = Ni, is large, and metallic layers can be formed by transition metals, lanthanides, actinides, alkaline earths, etc. Many of the compounds are magnetic, when X forms the magnetic sublattice, and the resulting frustration is identical to the ideal kagome model. A known but little studied representative of this family is CrRhAs^{37–40}. We have chosen it as an example to perform an extensive study of in-plane and out-of-plane magnetic interactions, using density functional

¹Department of Physics, Zhejiang University of Science and Technology, Hangzhou 310023, People’s Republic of China. ²Research Institute for Interdisciplinary Science, Okayama University, Okayama 700-8530, Japan. ³Department of Physics & Astronomy, George Mason University, Fairfax, VA 22030, USA. ⁴Quantum Science and Engineering Center, George Mason University, Fairfax, VA 22030, USA. ✉email: imazin2@gmu.edu

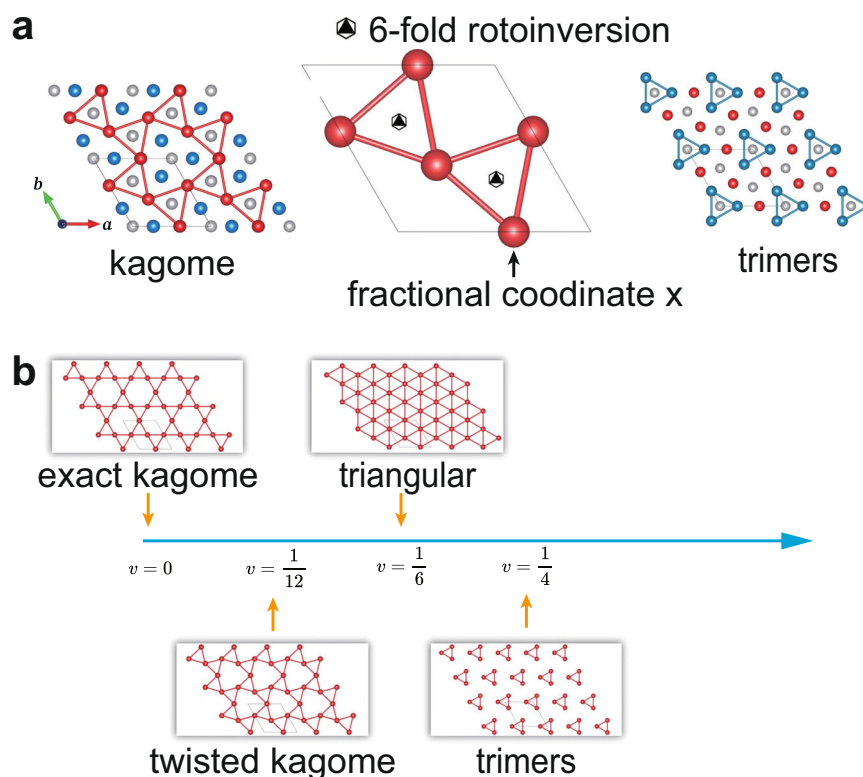


Fig. 1 Kagome lattice distortions within $P\bar{6}2m$ space group. **a** Two 6-fold rotoinversion axes in the unit cell of the $P\bar{6}2mXYZ$ compound (center). x is the fractional coordinate of the X atom indicated by an arrow. The left panel shows red atoms forming a kagome sublattice which is twisted by triangle rotations. The right panel shows blue atoms forming triangles. **b** The type of sublattice is uniquely determined by $v = x - 1/2$. When $v = 0$, the sublattice is exact kagome; when $|v| < 1/6$, it is a twisted kagome; when $|v| > 1/6$ it is trimers. The VESTA visualization program⁵² was used to generate this figure.

theory (DFT) calculations. We use the energies of spin spirals to extract the important parameters of a Heisenberg plus ring exchange Hamiltonian. We find that the second inplane exchange interaction clearly dominates over the first, leading to a spiral magnetic ground state. The dominant second-neighbor coupling is an interesting finding and shows that the twisted kagome lattice realized in CrRhAs and the entire family defined by its space group has remarkable properties beyond the known isotropic or distorted kagome lattice materials.

RESULTS

XYZ compounds with $P\bar{6}2m$ structure

In XYZ with $P\bar{6}2m$ space group, both X and Y sublattices are each characterized by one distortion parameter $v = x - \frac{1}{2}$, where x is the coordinate of the $3g$ ($3f$) Wyckoff position. The $3g$ and $3f$ positions differ only in the z coordinate, $1/2$ and 0 , respectively. The Z ions occupy two sublattices, $1b$ in the $3g$ plane, and $2c$ in the $3f$ plane. Increasing the absolute value of the distortion parameter $|v|$ makes the equilateral X triangles grow and rotate in the X_3Z plane. This takes the X sublattice from an ideal kagome lattice at $v = 0$ via a kagome lattice with rotated triangles and deformed hexagons for $0 < |v| < \frac{1}{6}$ and a perfect triangular lattice at $|v| = \frac{1}{6}$ to trimers for $|v| > \frac{1}{6}$. At increasing $|v|$, the triangular lattice of Z at the $1b$ position is enclosed by ever smaller X triangles. The v parameter has the same effect in the Y_3Z_2 plane with the difference that here, the Z in the $2c$ position form a honeycomb lattice. Thus, the connectivity in the two metal sublattices, X and Y , is different, which dramatically affects their magnetic properties. The compact triangles in the Y_3Z_2 plane tend to have considerable covalent bonding, and no, or little magnetism. The X ions, in

contrast, form only a moderately twisted kagome lattice (minimizing the Coulomb interaction with the ligand in the center), and are likely to have magnetism which can be frustrated in case of antiferromagnetic interactions.

We have inspected the $P\bar{6}2mXYZ$ compounds on the materials project website⁴¹ and organized some potentially magnetic ones into convenient tables, shown in Supplementary Note 1, Supplementary Tables 1 to 3. We found a number of XYZ compounds with significant magnetism, where magnetic kagome atoms can be Ce, Cr, Eu, Ho, Dy, Fe, Gd, Mn, Np, Pu, or U.

CrRhAs

We used a projector augmented wave basis as implemented in the Vienna ab initio simulation package (VASP)^{42–44} to perform noncollinear magnetic calculations—when needed, with individual constraints. We use all electron calculations with the full potential local orbital (FPLO) basis⁴⁵ to plot band structure and Fermi surface. The generalized gradient approximation (GGA) in the Perdew–Burke–Ernzerhof variant (PBE)⁴⁶ was used as the exchange–correlation potential.

We base our calculations on the crystal structure of CrRhAs determined by Deyris et al.⁴⁷ (ICSD 43919) with $a = b = 6.384(1)$ Å and $c = 3.718(1)$ Å. The internal atomic positions of CrRhAs were relaxed in VASP while keeping lattice parameters fixed. The optimized structural parameters are shown in Table 1, and will be used from now on.

Magnetic pattern analysis

In the following, we will infer magnetic couplings between Cr atoms (as shown in Fig. 2a) based on energies of different magnetic patterns on the Cr sublattices. In Fig. 2b, we define the

three sublattices Cr1, Cr2, Cr3 of the kagome lattice. Arrows of different colors indicate the 1st to 4th in-plane nearest neighbor Cr atoms to a reference Cr1 atom. Each arrow associated with a Heisenberg term $J_n \mathbf{s}_i \cdot \mathbf{s}_j$ where J_n means nth in-plane nearest Heisenberg coupling and $\mathbf{s}_{i=1,2,3}$ are normalized spin operators for Cr1, Cr2, Cr3. The polar angles of moments are assumed to be $\phi(1), \phi(2), \phi(3)$ for Cr1, Cr2, and Cr3, respectively. Figure 2a illustrates the connectivity of the J_n networks, with the same color convention as in Fig. 2b.

Table 1. GGA optimized fractional coordinates of CrRhAs.

Atom	Wyckoff	x	y	z
Cr	3g	0.6017	0	0.5
Rh	3f	0.2641	0	0
As1	1b	0	0	0.5
As2	2c	1/3	2/3	0

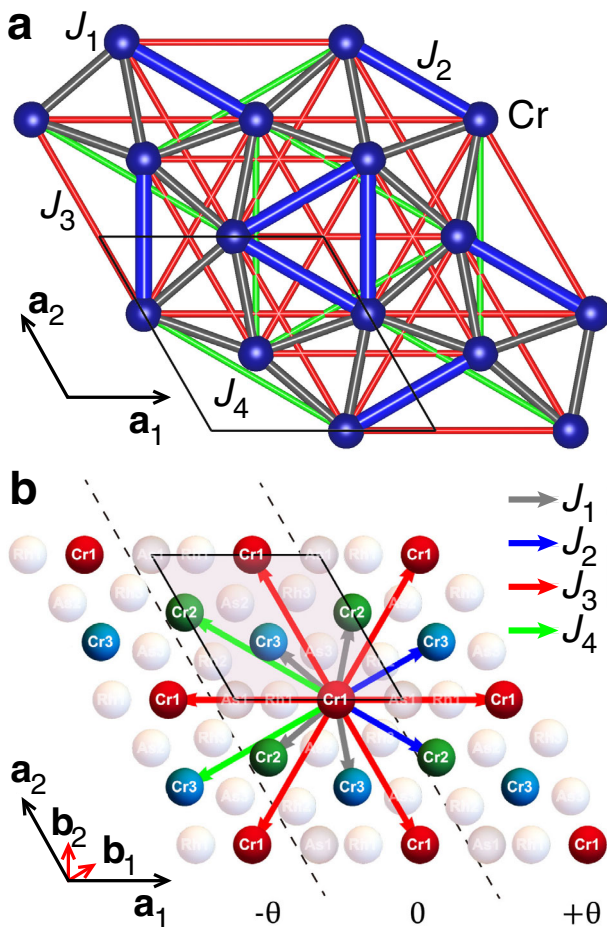


Fig. 2 Exchange paths and sublattice connectivity for CrRhAs. **a** Twisted kagome lattice formed by Cr in CrRhAs, with 1st to 4th in-plane nearest neighbor exchange interaction marked by different colors. The unit cell contains three symmetry equivalent Cr, which we denote Cr1, Cr2, and Cr3. **b** Noncollinear and spiral calculations are set up focusing on Cr1, Cr2, and Cr3 (red, green and blue) sublattices. Connectivity is highlighted for the Cr1 sublattice. The dashed lines cut the lattice into stripes corresponding to different spiral angles.

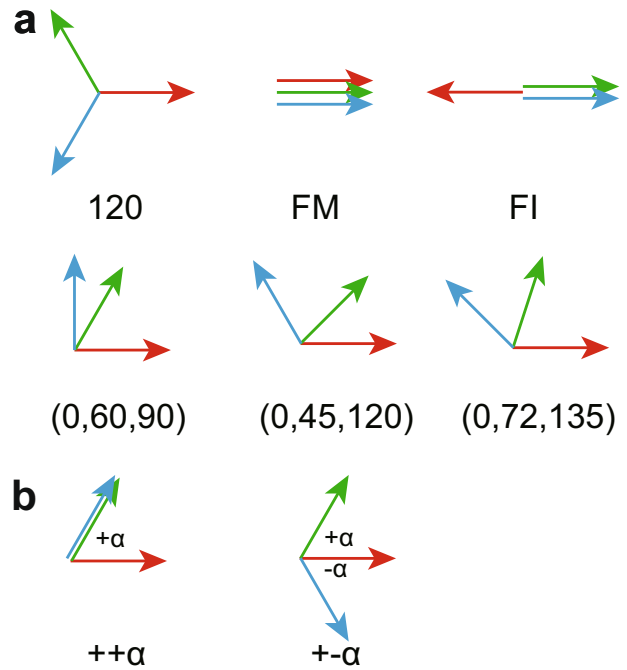


Fig. 3 Spin configurations for spirals and noncollinear calculations. **a** Six spin configurations within a unit cell considered in spin spiral calculations. Red, green, and blue arrows indicate the moment directions of Cr1, Cr2, and Cr3, respectively. **b** Spin configurations of noncollinear $++\alpha$ and $+-\alpha$. Red, green, and blue vector are spin moments of Cr1, Cr2, and Cr3 sublattice respectively.

Table 2. $\phi(1), \phi(2), \phi(3)$ (in degrees) for the six different spin spirals.

Spin configuration	$\phi(1)$	$\phi(2)$	$\phi(3)$
120	0	120	240
FM	0	0	0
FI	180	0	0
(0,60,90)	0	60	90
(0,45,120)	0	45	120
(0,72,135)	0	72	135

We will discuss spin spirals propagating along different directions and with six cases of spin configurations within a unit cell defined as 120, FM, FI, (0,60,90), (0,45,120), (0,72,135) as shown in Fig. 3a. The $\phi(1), \phi(2), \phi(3)$ for each case are listed in Table 2. Besides, we also discuss periodic magnetic patterns with varying angle α as defined in Fig. 3b.

The total energy of a magnetic pattern on Cr sublattices can be written as

$$H = E_0 + H_{\text{Heisenberg}} + H_{\text{ring}} \quad (1)$$

where $H_{\text{Heisenberg}}$ is defined as

$$H_{\text{Heisenberg}} = \sum_{i<j} J_{ij} \mathbf{s}_i \cdot \mathbf{s}_j \quad (2)$$

Here, the $\mathbf{s}_i = \frac{1}{S} \mathbf{S}_i$ are magnetic moment vectors normalized to 1. We write the exchanges in the kagome plane as $J_{ij} = J_1, J_2, \dots$ where 1, 2, ... correspond to increasing bond length (i.e., coordination shell). Exchange between the kagome layer and the next layer above and below are $J_{ij} = J'_0, J'_1, J'_2, \dots$, again sorted by distance (J'_0 is straight up or down). $J_{ij} = J''_0, J''_1, J''_2, \dots$ are bonds connecting second layers, and so on. The

identification of all bonds by Cr–Cr distance is provided in Supplementary Note 2.

H_{ring} is the ring exchange on a Cr triangle defined as

$$H_{\text{ring}} = L_1 \sum_{\Delta_1} \mathbf{s}_i \cdot \mathbf{s}_j + L_2 \sum_{\Delta_2} \mathbf{s}_i \cdot \mathbf{s}_j \quad (3)$$

where

$$\sum_{\Delta_1 \text{ or } \Delta_2} = (\mathbf{s}_1 \cdot \mathbf{s}_2)(\mathbf{s}_2 \cdot \mathbf{s}_3) + (\mathbf{s}_1 \cdot \mathbf{s}_3)(\mathbf{s}_3 \cdot \mathbf{s}_2) + (\mathbf{s}_2 \cdot \mathbf{s}_1)(\mathbf{s}_1 \cdot \mathbf{s}_3) \quad (4)$$

Here, summation over Δ_1 or Δ_2 means that $\mathbf{s}_{i=1,2,3}$ are the three moments of Cr1, Cr2, Cr3 that form 1st or 2nd nearest neighbor Cr triangle (red or blue triangles in Fig. 2a, respectively). L_1 and L_2 are the corresponding triangle ring exchange strengths.

With the above definitions, we can rewrite the total energy in Eq. (5) as

$$E = E_0 + L_1 D_1 + L_2 D_2 + \left(\sum_i J_i C_i + \sum_i J'_i C'_i + \dots \right) \quad (5)$$

where C_i, C'_i, D_1, D_2 are summations of terms like $\mathbf{s}_i \cdot \mathbf{s}_j$ and $(\mathbf{s}_i \cdot \mathbf{s}_j)(\mathbf{s}_j \cdot \mathbf{s}_k)$ that depend on magnetic patterns.

Spin spiral configurations

Spin spirals were modeled using the generalized Bloch theorem⁴⁸, as implemented in VASP. We calculated various spin spiral configurations for CrRhAs in order to get consistent information about the magnetic coupling between Cr ions in CrRhAs. A spin spiral is determined by a propagation vector \mathbf{q} within the first Brillouin zone of the reciprocal space lattice. We mainly considered $(q_x, 0, 0)$ and $(0, 0, q_z)$ spirals.

The $(q_x, 0, 0)$ spirals are propagating along the reciprocal \mathbf{b}_1 direction, which is shown in Fig. 2b. To understand the connectivity in these spirals, we can divide the lattice into stripes (dashed lines in Fig. 2b) running along the unit cell vector \mathbf{a}_2 , which is perpendicular to \mathbf{b}_1 . From one stripe to the next, all moments are rotated by the angle $\theta_x = \mathbf{q} \cdot \mathbf{a}_1$. There is an additional freedom of choosing Cr moment directions $\phi(1), \phi(2), \phi(3)$ within the unit cell, which generates different spin configurations. We considered six types of $(q_x, 0, 0)$ spin spirals, labeled as $(120)[q00]$, $(\text{FM})[q00]$, $(\text{FI})[q00]$, $(0, 60, 90)[q00]$, $(0, 45, 120)[q00]$, $(0, 72, 135)[q00]$ and corresponding $(0, 0, q_z)$ spirals labeled by replacing $[q00]$ with $[00q]$. For $(0, 0, q_z)$, a spiral propagates along the \mathbf{a}_3 direction, which is much simpler. All moments in a horizontal plane have the same spiral angle, and in the next plane along the \mathbf{a}_3 direction, they rotate by $\theta_z = \mathbf{q} \cdot \mathbf{a}_3$. Explaining the energetics of such spirals requires out of plane exchange couplings.

Simple, if tedious, calculation renders a Heisenberg Hamiltonian that is a linear form in J 's and L 's, with the coefficients C_i and D for general $(q_x, 0, q_z)$ spin spirals, as shown in Supplementary Note 3. For each spiral of the 120, FI, and FM cases, we performed spiral total energy calculations from spiral angle 0 to π , because their energy is symmetric with respect to spiral angle π up to J_4 . For the other cases, $(0, 60, 90)$, $(0, 45, 120)$, $(0, 72, 135)$, we calculated the full spiral angle range 0 to 2π .

Noncollinear periodic calculations

We also consider simple periodic cases where the three Cr sublattices have three different noncollinear spin directions, as shown in Fig. 3b, and where we vary the angle α . Taking the spin direction of Cr1 as reference, in the $++\alpha$ case the spin directions of Cr2 and Cr3 are rotated by the same angle $+\alpha$, while in the $+-\alpha$ case, the spin direction of Cr2 and Cr3 are rotated by $+\alpha$ and $-\alpha$, respectively. The energy versus α curves and their fittings to different orders of cosine are shown in Supplementary Note 4.

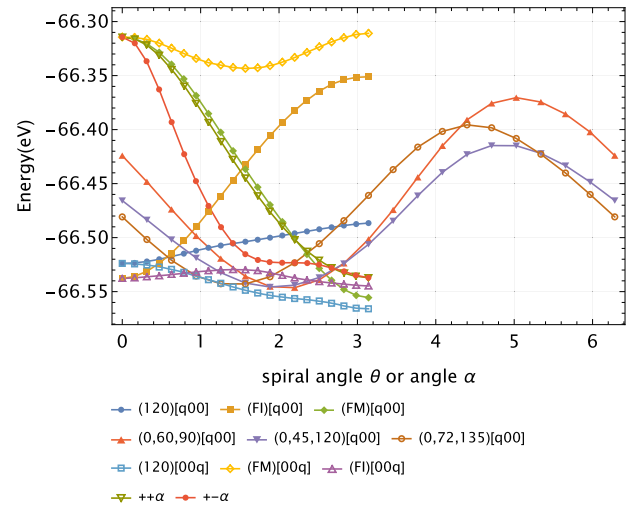


Fig. 4 Energies for spiral and noncollinear spin configurations as function of angle. Energy curves of six $(q, 0, 0)$ spirals, three $(0, 0, q)$ spirals, $++\alpha$ and $+-\alpha$.

If the magnetic interaction is dominated by Heisenberg-type contributions, we would expect that a simple $\cos(\alpha)$ will fit the $++\alpha$ curve well. As we can see from Supplementary Fig. 2, the fit is indeed not bad with $\cos(\alpha)$ only, but after adding $\cos(2\alpha)$ it becomes much better. For the $+-\alpha$ case, we would expect $\cos(\alpha)$ plus $\cos(2\alpha)$ will fit well. However, it turns out that fitting to the order of $\cos(2\alpha)$ still has a large discrepancy with the calculated energies, and by adding a $\cos(3\alpha)$ term, two curves immediately snap together. So it is clear that explaining the $+-\alpha$ curve needs the $\cos(3\alpha)$ term.

One probable explanation is that there is ring exchange between three Cr atoms. For the spins $\mathbf{s}_1, \mathbf{s}_2, \mathbf{s}_3$ of $\text{Cr}_{i=1,2,3}$, a ring exchange interaction is proportional to $(\mathbf{s}_1 \cdot \mathbf{s}_2)(\mathbf{s}_2 \cdot \mathbf{s}_3) + (\mathbf{s}_1 \cdot \mathbf{s}_3)(\mathbf{s}_3 \cdot \mathbf{s}_2) + (\mathbf{s}_2 \cdot \mathbf{s}_1)(\mathbf{s}_1 \cdot \mathbf{s}_3)$. In the $+-\alpha$ case, this will introduce $\cos(\alpha)\cos(2\alpha)$ and $\cos(\alpha)^2$ terms, and $\cos(\alpha)\cos(2\alpha)$ is equivalent to $\frac{1}{2}(\cos(3\alpha) + \cos(\alpha))$, so that $\cos(3\alpha)$ emerges as soon as we consider ring exchange. For the $++\alpha$ case, the ring exchange term introduces additional $\cos(\alpha)^2$ contributions that also improves the fit.

Fitting all energy curves

Energies of six $(q_x, 0, 0)$ spirals, three $(0, 0, q_z)$ spirals, $++\alpha$ and $+-\alpha$ are shown in Fig. 4. Note that we have intentionally shifted the curves of $++\alpha$ and $+-\alpha$ up to align with $(\text{FM})[q00]$ and $(\text{FM})[00q]$ at $\theta = 0$, because due to the internal realization of VASP, energies of noncollinear and spiral calculations have a constant shift. From Fig. 4 The 120[00q] with $\theta = \pi$ has the lowest energy. This means that the interlayer coupling is AFM, and moments on Cr atoms on the same triangle tend to form 120 degree angles with each other.

Now we have 9 spiral curves plus 2 noncollinear curves with variable angle as shown in Fig. 4, which can be fit to Eq. (5), using Supplementary Table 5. It appears that only a subset of J 's are linearly independent; furthermore, some longer-range couplings, while they can formally be extracted by the fit, come out very small and improve the fit only marginally. A choice of $E_0, J_1, J_2, J_3, J_4, J'_0, J'_1, J''_0, J''_1, L$ as a physically meaningful Hamiltonian gives good overall fits as shown in Fig. 5.

From this fitting result, we found that J_2 is the dominant exchange interaction. It is an antiferromagnetic coupling, and interestingly it is 10 times larger than the second largest ferromagnetic exchange interaction J_1 . What is more, J_3, J_4 are also of the same order of magnitude as J_1 . The nearest and next

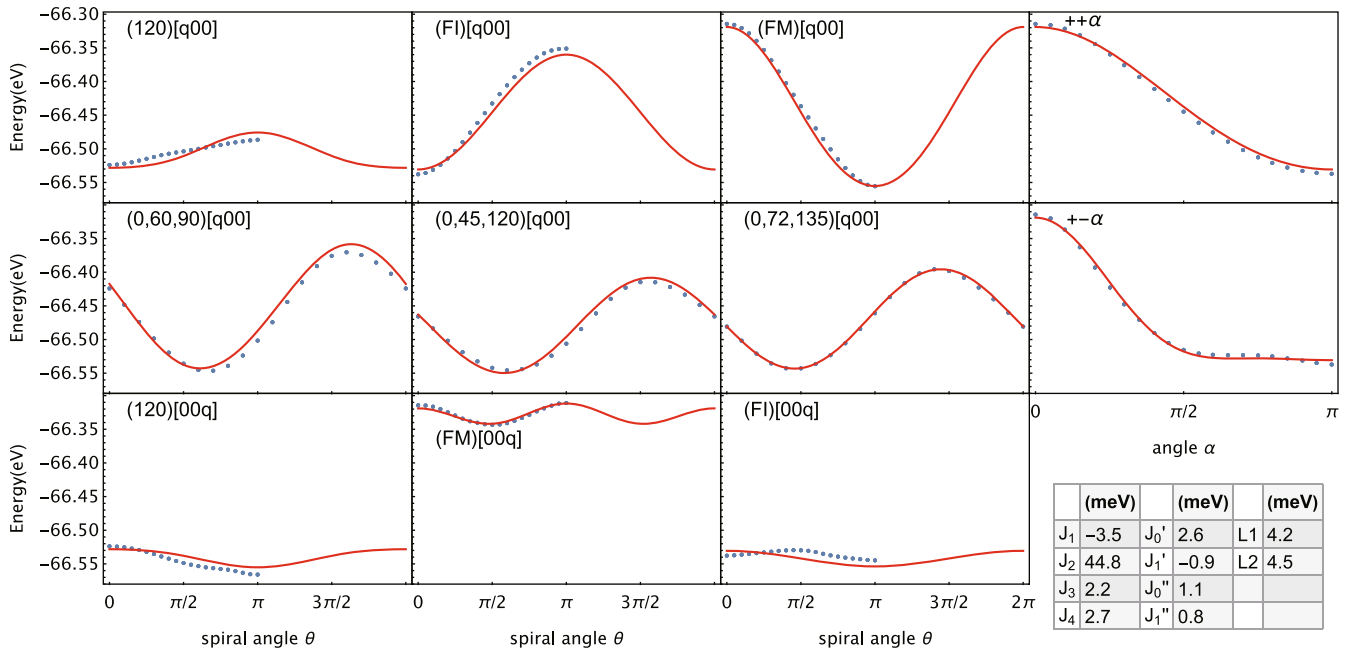


Fig. 5 Heisenberg plus ring exchange Hamiltonian fit of spiral and noncollinear DFT energies. Least square fit of six $(q_x, 0, 0)$ spirals, three $(0, 0, q_z)$ spirals, $++\alpha$ and $+-\alpha$ to the Heisenberg Hamiltonian including four in-plane neighbors, two neighbors in the first and second interplanar interactions, and the nearest neighbor ring exchange, as discussed in the text. Blue symbols are calculated DFT energies. Red curves are the least squares fit with the parameters shown on the right.

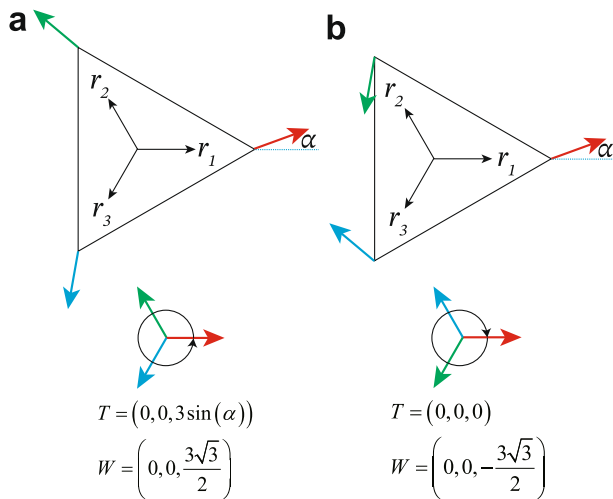


Fig. 6 Toroidal moment and vector chirality on a triangle of spins. There are two topologically different 120° magnetic patterns. Red, green, and blue vectors are spin moments of Cr1, Cr2, and Cr3 sublattices, respectively. Note that the left pattern (a) has an α dependent, usually non-zero toroidal moment $T = 3 \sin \alpha$ (assuming the black vectors r_i and magnetic moments have unit lengths), which can be continuously varied from 3 to -3 by rotating the spin space with respect to the coordinate space, while the right pattern (b) has always $T = 0$, and that is not affected by the spin-space rotation. The left pattern (a) has positive, the right pattern (b) negative vector chirality.

nearest interlayer coupling is antiferromagnetic. Thus, we find a Heisenberg Hamiltonian with clearly dominating antiferromagnetic interactions, in agreement with the fact that experimentally CrRhAs was found to order antiferromagnetically with a Neel temperature of $T_N = 165 \text{ K}$ ³⁷. Considering the hierarchy of exchange couplings, we expect the J_2 triangles to order in a 120 degree state. The second largest ferromagnetic J_1 couplings

cannot be exactly satisfied because of J_1 - J_2 - J_1 triangles, and they already introduce some frustration. The smaller in-plane couplings J_3 and J_4 also contribute to frustration. Interestingly, even though the interlayer distances of CrRhAs are small, interlayer exchange is much smaller than in-plane exchange, and the material is magnetically rather two-dimensional.

Furthermore, the ring exchange term is indispensable for good fits of the DFT energies and is substantial at 12% of the dominant exchange interaction. Note that we can directly compare Heisenberg and ring exchange terms as we are using unit moments. As shown in Supplementary Fig. 3, without ring exchange, there are discrepancies between fitted and original data curves as large as 20 meV for (120)[q00] and (120)[00q] at $\theta = 0$, and similarly for $+-\alpha$.

Discussion of the emerging Hamiltonian

The Hamiltonian derived in the previous section is quite unusual. First, it is dominated by the large AF 2nd nearest-neighbor interaction (blue bonds shown in Fig. 2a). These bonds form isolated triangles, all oriented in the same way. Each triangle, obviously, orders in a 120° fashion, and is formed by the three different Cr, Cr1, Cr2, and Cr3. Let us first for simplicity assume an XY model, so all spins lie in the ab plane (Fig. 7). There are two different ways to produce this order, illustrated in Fig. 6, differing by the sign of their vector chirality $\mathbf{W} = \mathbf{M}_1 \times \mathbf{M}_2 + \mathbf{M}_2 \times \mathbf{M}_3 + \mathbf{M}_3 \times \mathbf{M}_1$ on the dominant J_2 triangles. We use positive or negative vector chirality to distinguish between the two states (see Fig. 6). Toroidal moment $\mathbf{T} = \sum_{i=1}^3 \mathbf{r}_i \times \mathbf{M}_i$ is usually non-zero for the state with positive vector chirality while it is always zero for the state with negative vector chirality. After one or the other type is selected, each blue triangle is fully determined by one of its spins (let's say, by the Cr1 spin). Then the lattice of the blue triangles is equivalent to a triangular lattice shown in red (see Fig. 7).

Let us now determine the effective Hamiltonian for this lattice: consider two blue triangles shifted along a . The Cr1 on the right is connected to Cr2' and Cr3' on the left, where "' means the atoms from the left triangle. The corresponding contribution to energy is

$J_1 \mathbf{S}_1 \cdot (\mathbf{S}'_2 + \mathbf{S}'_3) = -J_1 \mathbf{S}_1 \cdot \mathbf{S}'_1$. Thus, the FM n.n. interaction gives rise to an AF interaction for this red bond, which needs to be added to the, also AF, J_3 .

Let us now evaluate the interaction along \mathbf{a}_2 . By the same token, the coupling between the corresponding Cr2 atoms is also $J_{\text{eff}} = J_3 - J_1$. Since the moment of Cr2 is just the moment of Cr1 in the same gray triangle rotated by $2\pi/3$, it is the same as adding J_{eff} along \mathbf{a}_2 for the Cr1 atoms (note that in principle we could rotate

spins in the opposite directions when shifting along \mathbf{a}_2 compared to shifting along \mathbf{a}_1 , but that would have been energetically unfavorable).

Thus, we get a unique ground state, where the spins on the blue sublattice, which are of three different colors, form a 120° -lattice, and each color within itself also forms 120° -lattices. Next, let us look at the gray triangles. Their centers are denoted by green and orange dots. They form a perfect honeycomb lattice, but it partitions (as the honeycomb lattice is bipartite) into two (triangular again) subsets (green and orange), one sporting FM triangles and the other 120° -triangles. Note that in terms of the *toroidal* moments it is reversed: the former subset has zero toroidal moments, while the latter non-zero ones. Note that the J_4 interaction, comparable with J_3 (but considerably smaller than $J_{\text{eff}} = J_3 - J_1$) is also satisfied as well as it is possible for a triangular lattice, i.e., with 120° angles.

If we now select the other pattern with a positive vector chirality on the dominant J_2 (blue) triangles, we end up with an alternative structure, strictly degenerate with the first one (Fig. 7b).

To summarize, the effective model can be mapped onto a triangular lattice where each site is characterized by a Heisenberg-spin variable (let us call it Σ , which shows the spin direction of the selected corner (Cr1, in this case), and another unit-length axial vector, Ω , showing the sense of the rotation in a given blue triangle (i.e., rotations from Cr1 to Cr2 to Cr3 by $2\pi/3$ proceed around the axis Ω , and the sense of the rotation is given by the sign of Ω). The interaction between the effective spins Σ is also Heisenberg, AF, and much smaller than the interactions inside a trimer. Note that while *magnetically* the system partitions naturally into trimers, *electronically* it maintains full connectivity, so electronic flat bands arising in breathing kagome systems with a physical trimerization¹⁷ do not appear here. This leads to a standard triangular Heisenberg order, which can also be characterized by a Heisenberg spin variable, \mathbf{S}_0 , which can be selected as the value Σ_0 at the origin, and another unit-length rotation vector, ω . At the end, the entire long-range magnetic order can be described by one Heisenberg spin Σ_0 and two axial rotational vectors Ω and ω . This is to be contrasted with the less-degenerate standard triangular lattice, which can be uniquely described by the origin spin and one rotational vector.

Consideration of the second type of ordering, the one with positive vector chirality on the J_2 triangles, proceeds along the same lines. The results are summarized in Tables 3 and 4. The main difference is that in the former case half of the nearest neighbor triangles have non-zero toroidicity, which however averages to zero, while in the latter the same is true for the second-neighbor trimers.

Adding the ring exchange which we found to be sizeable does not alter this ground state. Indeed, it is easy to show that if an AF coupling on a triangle $J > 7L/2$ the ground state is not altered by adding the ring exchange. Finally, interaction along the c axis is strongly frustrated, with comparable J'_0, J'_1 , and J''_1 , which can lead,

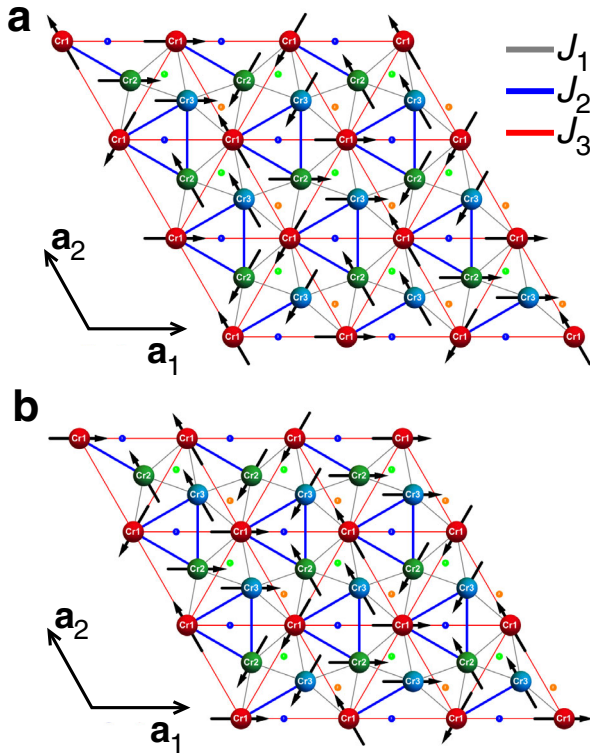


Fig. 7 Possible ground states for dominant Heisenberg interactions of CrRhAs. Two possible 2D ground states of the reduced magnetic Hamiltonian including J_1 to J_4 interactions (note that the ground state is highly degenerate). The blue bonds indicate the strongest exchange coupling (AF) in the system (J_2), which generates 120° trimers, the gray bonds the nearest neighbor triangles, and the red one effective inter-trimer AF interaction, numerically equivalent to $J_3 - J_1$. Note that while in the ground state the blue trimers are ordered in a 120° fashion, and the red bonds network also assumes a 120° order, the two orders, in this model, are not correlated and may have different ordering planes and toroidal moments. The blue dots indicate centers of the blue trimers, and the green and orange ones centers of the n.n. triangles. The top diagram (a) corresponds to an order with negative vector chirality on the blue triangles, the bottom one (b) to one with positive vector chirality.

Label	Triangles	Connectivity	Effective coupling	Net moment	Toroidicity	Vector chirality ($\ \mathbf{z}$)
a	Nearest neighbors	Honeycomb	J_1	3	0	0
	Sublattice 1			0	$[-3,3], \langle \dots \rangle = 0$	$3\sqrt{3}/2$
	Sublattice 2			0	$[-3,3], \langle \dots \rangle = 0$	$-3\sqrt{3}/2$
b	2nd neighbors	Trimers	J_2	0	0	$-3\sqrt{3}/2$
c	Centers of the "b" triangles ^a	Triangular	$J_3 - J_1$	0	$[-3,3], \langle \dots \rangle = 0$	$\langle \dots \rangle = 0$
d	4th neighbors	Trimers	J_4	0	0	$-3\sqrt{3}/2$

^aEquivalent to the 3rd neighbor triangles. For the purpose of this table, the two ordering planes are assumed parallel, $\Omega \parallel \omega$, so that the scalar chirality is always zero.

Table 4. Same as Table 3, for the spin configuration with positive vector chirality on the dominant J_2 triangle.

Label	Triangles	Connectivity	Effective coupling	Net moment	Toroidicity	Vector chirality ($\ \mathbf{z}$)
a	Nearest neighbors	Honeycomb	J_1			
	Sublattice 1			3	0	0
	Sublattice 2			0	0	$-3\sqrt{3}/2$
b	2nd neighbors	Trimers	J_2	0	$[-3,3], \langle \dots \rangle = 0$	$3\sqrt{3}/2$
c	Centers of the “b” triangles ^a	Triangular	$J_3 - J_1$	0	$[-3,3], \langle \dots \rangle = 0$	$\langle \dots \rangle = 0$
d	4th neighbors	Trimers	J_4	0	$[-3,3], \langle \dots \rangle = 0$	$3\sqrt{3}/2$

^aEquivalent to the 3rd neighbor triangles. For the purpose of this table, the two ordering planes are assumed parallel, $\mathbf{\Omega} \parallel \boldsymbol{\omega}$, so that the scalar chirality is always zero.

generally speaking, to spiral states propagating in this direction (given the higher coordination number for the last two).

While these two states have been discussed above in terms of supercells, one can notice that they also form spin spirals of a sort. Namely, the first one can be described, using our notations, as the $(120, 0, 0)[4\pi/3, 4\pi/3, 0]$ spiral, and the second as the $(0, 120, 120)[2\pi/3, 2\pi/3, 0]$ one. Note that in this Hamiltonian, the two spirals are degenerate, and have not been included in our previous calculations and fitting. Thus, these two states are true predictions and can be explicitly verified. Indeed, we found that, as predicted by the model Hamiltonian, they are (a) degenerate within computational accuracy and (b) 25.6 meV below the lowest-energy state found in the original calculations (namely, the standard 120° structure alternating antiferromagnetically between the planes.)

The last observation relates to the situation that, when the ordering planes are not parallel, $\mathbf{\Omega} \nparallel \boldsymbol{\omega}$, a finite local scalar chirality can be acquired, leading, for instance, to a topological Hall effect. This opens the door to a fluctuation-induced topological Hall effect at finite temperature²⁸; however, further analysis is outside the scope of this paper.

Comparison with experiment

Experimental information on this material is, basically, limited to four papers from T. Kaneko and co-authors^{37–40}. It has been established that CrRhAs experiences an antiferromagnetic transition, with the Néel temperature reported at $T_N = 165$ K^{37–39} or 172 K⁴⁰. The antiferromagnetic order has not been established. Interestingly, the magnetic susceptibility measured in an interval between T_N and room temperature is distinctly non-Curie-Weiss (CW). In the first publication, ref. 37, it was fitted to the CW law, $\chi = C/(T - \Theta) + \text{const}$, but with a background of 1.47×10^{-3} emu/mole, which, if interpreted as Pauli susceptibility, corresponds to 45 states/(eV · f.u.), or to an ad hoc formula $\chi = C'/(T - \Theta')^\gamma$, with $C' = 4.8 \times 10^{-3}$ emu K/mole, $\Theta' = 20$ K and $\gamma = 0.16$. In a later paper, ref. 38, the same formula was used with $\chi = C'/(T - \Theta')^\gamma$, with $C' = 3.2 \times 10^{-2}$ emu K/mole, $\Theta' = -16$ K and $\gamma = 0.44$, presumably, due to a different protocol for the background removal. Either way, $\chi^{-1}(T)$ is strongly nonlinear and its slope gets smaller with the temperature. If one defines “instantaneous” CW parameters as $C(T) = 1/(d\chi^{-1}(T)/dT)$ and $\Theta(T) = T - C(T)/\chi(T)$, then $\Theta(T)$ is becoming increasingly antiferromagnetic with temperature, and $C(T)$ also grows, corresponding to increasingly large effective moments.

All these observation, as strange as they may seem on the first glance, find natural explanations in our Hamiltonian and proposed ground state. Indeed, the former is dominated by the very strong J_2 interaction, which itself corresponds to a temperature scale of $2J_2$ (2 for the coordination number) of the order of 1000 K, or if converted to the CW temperature and assuming spin 3/2 and the quantum factor $(S + 1)/S = 5/3$, corresponds to $T_{CW} = -578$ K. This indicates that at room temperature the isolated trimers

formed by the J_2 bonds are still strongly correlated, forming complexes with strongly suppressed net magnetic moment. As a result, the true CW regime is not attained until $T \gtrsim 600$ K, and the observed behavior is nothing but a gradual crossover from the fully correlated trimers with the effective moment $m_{\text{eff}} \ll 1\mu_B$ and T_{CW} defined by the other (besides J_2) interactions in the system (which is on the order of -72 K), and the very high-temperature regime, not reached in the reported experiments, where $m_{\text{eff}} \sim \sqrt{3 \cdot 5} = 3.87\mu_B$, and $T_{CW} \sim -650$ K. Finally, the relatively small value of T_N compared to the high T_{CW} temperature finds a natural explanation in the fact that the intra-trimer ordering that does happen at high temperature is not related to the temperature at which the individual triangles order with respect to each other; the latter is determined by the much weaker inter-trimer interactions. In fact, an upper boundary on the mean-field transition temperature can be derived by taking all interactions but J_2 with the same sign (remember that, for instance, J_1 and J_3 , although they are of the opposite signs, cooperate in the suggested ordering). This gives an estimate for the maximally possible ordering temperature of 346 K. The experimental number is right between the lower estimate of 72 K and this upper bound.

Electronic structure of CrRhAs

Finally, we turn our attention to the band structure and Fermi surface of CrRhAs. We use GGA calculations with the FPLO basis to determine both nonmagnetic (Fig. 8a) and examples of magnetic band structures (Fig. 8b, c). At the Fermi level, most of the density of states derives from Cr 3d, with only small Rh 4d and very small As 3p contributions (Fig. 8a). In the non-magnetic bands, a Dirac point at the K point can be seen about 0.4 eV above the Fermi level but flat bands are hard to make out. CrRhAs remains metallic in both ferromagnetic and ferrimagnetic states (Fig. 8b, c) as well as in antiferromagnetic spin configurations (not shown). However, DOS at E_F is substantially lower in magnetic compared to non-magnetic states. The non-magnetic Fermi surface (see Fig. 8d for cuts, Fig. 8h, i for 3D plots) has some cylinder-like 2D features but also significant variation along k_z . The FS for the ferromagnetic solution (Fig. 8e, f) is not much simpler.

DISCUSSION

We studied one member of a large family of XYZ compounds with space group $P\bar{6}2m$ that contains twisted kagome and trimerized (distorted triangular) lattices. As many as 70 of them have significant magnetism on a kagome lattice, and despite the distorted geometry, the magnetic interaction Hamiltonian remains the same as ideal kagome at the nearest neighbor level, which makes this series of compounds a fertile playground for kagome physics. We used CrRhAs as an example to study different spin spiral and noncollinear energies.

To this end, we have calculated within the density functional theory the total energies of six different in-plane spin spirals, three

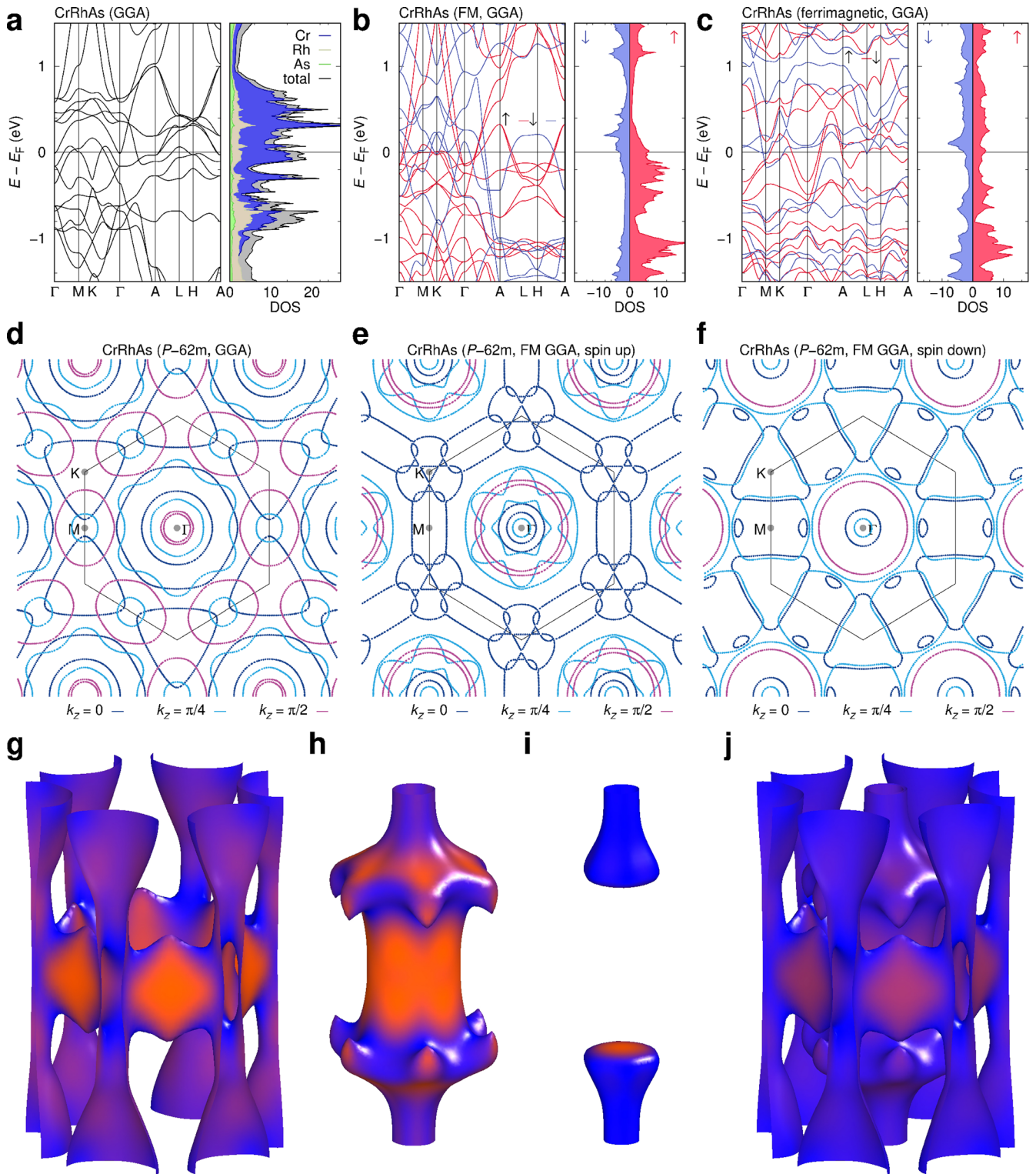


Fig. 8 GGA electronic structure of CrRhAs. **a** Nonmagnetic, **b** ferromagnetic, and **c** ferrimagnetic bands with corresponding densities of states. **d** $k_x - k_y$ plane cuts of the Fermi surface for three different values of k_z . **e**, **f** The same for the ferromagnetic solution. **g–j** 3D contour plots of the nonmagnetic Fermi surface; **g–i** are three individual FS sheets, and **j** shows all of them together. In **g–j**, color indicates Fermi velocity where blue is low, orange high.

different out-of-plane spirals, and two continuously varying noncollinear magnetic arrangements with the $\mathbf{q} = 0$ periodicity, a total of more than 230 first principle calculations. Based on these data, we generated a magnetic Hamiltonian that fits all these energies reasonably well (with max deviation within 15 meV).

Interestingly, the resulting Hamiltonian was rather unusual in several aspects: first, we found that Heisenberg exchange interactions could not provide a satisfactory fit; adding ring exchange terms proved indispensable, especially for the two $\mathbf{q} = 0$ sets of calculations. Second, we found that the nearest neighbor

exchange coupling was ferromagnetic, and thus not frustrated, but the leading (by far) interaction was the next nearest neighbor antiferromagnetic coupling in the twisted kagome plane, which is frustrated and leads to a curious, and, to the best of our knowledge, never discussed before magnetic Hamiltonian. The ground state of this Hamiltonian is controlled by independent triangles of a certain vector spin chirality, either positive or negative, but the same for all triangles, and varying toroidicity between these triangles. Furthermore, it has a potential to develop, either statically due to spin-orbit coupling, or dynamically through topological field fluctuations, scalar spin chirality, and topological Hall effect. These possibilities, however, go beyond the scope of our paper.

We hope that this study would motivate further experimental and theoretical research into this intriguing family, and particularly this specific system. An unexpected outcome is that the twisted kagome lattice of XYZ compounds in $\bar{P}62m$ space group with magnetic X can realize unusual highly frustrated Hamiltonians that are not known in pristine or distorted kagome materials and hold the promise of future discoveries and surprises.

METHODS

Structure preparation

The structure relaxation and noncollinear magnetic calculations of CrRhAs were performed using the Vienna ab initio simulation package (VASP)^{42–44}. The projector augmented wave (PAW) potentials^{49,50} with the generalized gradient approximation (GGA) exchange–correlation potential in the Perdew–Burke–Ernzerhof variant (PBE)⁴⁶ were used in all calculations. Explicitly, Cr_pv, Rh_pv, As_d potentials are used.

The internal atomic positions of CrRhAs were relaxed with lattice parameters $a = b = 6.384(1)$ Å and $c = 3.718(1)$ Å kept fixed based on the experimental structure by Deyris et al.⁴⁷ (ICSD 43919) using Γ -centered mesh $6 \times 6 \times 9$ and energy cutoff 400 eV. The convergence criterion is that all forces are smaller than 0.01 eV/Å. The optimized structure was then used for noncollinear magnetic calculations.

Spin spiral calculations

Spin spirals were modeled using the generalized Bloch theorem⁴⁸, as implemented in VASP. The Γ -centered mesh was set to $8 \times 8 \times 12$, and the lower and upper limits of the energy cutoff were set to 380 and 480 eV. The moments of Cr atoms are initially set to $4\mu_B$, and only the directions of the moments in the unit cell are constrained during the self-consistent process. With different moment configurations together with different spiral propagation vectors \mathbf{q} , we calculated the total energies of different spin spirals of CrRhAs, and for each spin spiral, a corresponding Heisenberg Hamiltonian energy expression plus ring exchange terms involves different J_s . By keeping a limited set of J_s , we can obtain values for the exchange couplings and ring exchange via least squares fitting.

Electronic structure calculations

The band structures and Fermi surfaces were calculated using all-electron calculations with the full potential local orbital (FPLO) basis⁴⁵. As in VASP, GGA in the PBE variant was used as the exchange–correlation potential. Calculations are converged with a $24 \times 24 \times 24$ k mesh. For the ferrimagnetic state, we lower the space group symmetry from $P-62m$ to $Amm2$. We use an extended basis set to increase the precision⁵¹. The spin-orbit coupling, expected to be small here, was not included in these calculations.

DATA AVAILABILITY

The data that support the findings of this study are available from the corresponding author upon reasonable request.

CODE AVAILABILITY

The custom codes implementing the calculations of this study are available from the authors upon reasonable request.

Received: 10 November 2022; Accepted: 16 May 2023;

Published online: 07 June 2023

REFERENCES

- Zhou, Y., Kanoda, K. & Ng, T.-K. Quantum spin liquid states. *Rev. Mod. Phys.* **89**, 025003 (2017).
- Broholm, C. et al. Quantum spin liquids. *Science* **367**, eaay0668 (2020).
- Savary, L. & Balents, L. Quantum spin liquids: a review. *Rep. Prog. Phys.* **80**, 016502 (2016).
- Balents, L. Spin liquids in frustrated magnets. *Nature* **464**, 199–208 (2010).
- Shores, M. P., Nytko, E. A., Bartlett, B. M. & Nocera, D. G. A structurally perfect $S = 1/2$ kagomé antiferromagnet. *J. Am. Chem. Soc.* **127**, 13462–13463 (2005).
- Han, T.-H. et al. Fractionalized excitations in the spin-liquid state of a kagome-lattice antiferromagnet. *Nature* **492**, 406–410 (2012).
- Barthélemy, Q. et al. Specific heat of the kagome antiferromagnet herbertsmithite in high magnetic fields. *Phys. Rev. X* **12**, 011014 (2022).
- Fåk, B. et al. Kapellasite: a kagome quantum spin liquid with competing interactions. *Phys. Rev. Lett.* **109**, 037208 (2012).
- Iqbal, Y. et al. Paramagnetism in the kagome compounds (Zn, Mg, Cd) $\text{Cu}_3(\text{OH})_6\text{Cl}_2$. *Phys. Rev. B* **92**, 220404 (2015).
- Barthélemy, Q. et al. Local study of the insulating quantum kagome antiferromagnets $\text{YCu}_3(\text{OH})_6\text{O}_x\text{Cl}_{3-x}$ ($x = 0, 1/3$). *Phys. Rev. Mater.* **3**, 074401 (2019).
- Hering, M. et al. Phase diagram of a distorted kagome antiferromagnet and application to Y-kapellasite. *npj Comput. Mater.* **8**, 10 (2022).
- Guterding, D., Valentí, R. & Jeschke, H. O. Reduction of magnetic interlayer coupling in barlowite through isoelectronic substitution. *Phys. Rev. B* **94**, 125136 (2016).
- Feng, Z. et al. Gapped spin-1/2 spinon excitations in a new kagome quantum spin liquid compound $\text{Cu}_3\text{Zn}(\text{OH})_3\text{FBr}$. *Chin. Phys. Lett.* **34**, 077502 (2017).
- Billitewski, T., Zhitomirsky, M. E. & Moessner, R. Jammed spin liquid in the bond-disordered kagome antiferromagnet. *Phys. Rev. Lett.* **119**, 247201 (2017).
- Sheckelton, J. P., Neilson, J. R., Soltan, D. G. & McQueen, T. M. Possible valence-bond condensation in the frustrated cluster magnet $\text{LiZn}_2\text{Mo}_3\text{O}_8$. *Nat. Mater.* **11**, 493–496 (2012).
- Nikolaev, S. A., Solov'yev, I. V. & Streltsov, S. V. Quantum spin liquid and cluster mott insulator phases in the Mo_3O_8 magnets. *npj Quant. Mater.* **6**, 25 (2021).
- Haraguchi, Y. et al. Magnetic-nonmagnetic phase transition with interlayer charge disproportionation of Nb_3 trimers in the cluster compound Nb_3Cl_8 . *Inorg. Chem.* **56**, 3483–3488 (2017).
- Li, Y., Liu, C., Zhao, G.-D., Hu, T. & Ren, W. Two-dimensional multiferroics in a breathing kagome lattice. *Phys. Rev. B* **104**, L060405 (2021).
- Boyko, D., Saxena, A. & Haraldsen, J. T. Spin dynamics and Dirac nodes in a kagome lattice. *Ann. Phys.* **532**, 1900350 (2020).
- Sun, Z. et al. Observation of topological flat bands in the kagome semiconductor Nb_3Cl_8 . *Nano Lett.* **22**, 4596–4602 (2022).
- Liu, D. F. et al. Magnetic Weyl semimetal phase in a Kagomé crystal. *Science* **365**, 1282–1285 (2019).
- Owerre, S. A. Topological thermal Hall effect in frustrated kagome antiferromagnets. *Phys. Rev. B* **95**, 014422 (2017).
- Owerre, S. A. Weyl magnons in noncoplanar stacked kagome antiferromagnets. *Phys. Rev. B* **97**, 094412 (2018).
- Zhao, K. et al. Realization of the kagome spin ice state in a frustrated intermetallic compound. *Science* **367**, 1218–1223 (2020).
- Kang, M. et al. Dirac Fermions and flat bands in the ideal kagome metal FeSn. *Nat. Mater.* **19**, 163–169 (2020).
- Han, M. et al. Evidence of two-dimensional flat band at the surface of antiferromagnetic kagome metal FeSn. *Nat. Commun.* **12**, 5345 (2021).
- Ye, L. et al. Massive Dirac fermions in a ferromagnetic kagome metal. *Nature* **555**, 638–642 (2018).
- Ghimire, N. J. et al. Competing magnetic phases and fluctuation-driven scalar spin chirality in the kagome metal YMn_6Sn_6 . *Sci. Adv.* **6**, eabe2680 (2020).

29. Li, M. et al. Dirac cone, flat band and saddle point in kagome magnet YMn_5Sn_6 . *Nat. Commun.* **12**, 3129 (2021).
30. Zhang, H. et al. Topological magnon bands in a room-temperature kagome magnet. *Phys. Rev. B* **101**, 100405 (2020).
31. Wu, X. et al. Nature of unconventional pairing in the kagome superconductors AV_3Sb_5 (A=K,Rb,Cs). *Phys. Rev. Lett.* **127**, 177001 (2021).
32. Nie, L. et al. Charge-density-wave-driven electronic nematicity in a kagome superconductor. *Nature* **604**, 59–64 (2022).
33. Chen, K. Y. et al. Double superconducting dome and triple enhancement of T_c in the kagome superconductor CsV_3Sb_5 under high pressure. *Phys. Rev. Lett.* **126**, 247001 (2021).
34. Mielke, C. et al. Time-reversal symmetry-breaking charge order in a kagome superconductor. *Nature* **602**, 245–250 (2022).
35. Lacroix, C. Frustrated metallic systems: a review of some peculiar behavior. *J. Phys. Soc. Jpn.* **79**, 011008 (2010).
36. Siddiqui, S. A. et al. Metallic antiferromagnets. *J. Appl. Phys.* **128**, 040904 (2020).
37. Ohta, S., Kanomata, T. & Kaneko, T. Magnetic properties of CrRhAs and CrRuAs. *J. Mag. Mag. Mater.* **90–91**, 171–172 (1990).
38. Kanomata, T. et al. Magnetic properties of the intermetallic compounds $MM'X$ (M=Cr,Mn, M'=Ru,Rh,Pd, and X=P,As). *J. Appl. Phys.* **69**, 4639–4641 (1991).
39. Kaneko, T. et al. High-field magnetization in intermetallic compounds $MM'X$ (M=Mn, Cr; M'=Ru, Rh, Pd; X=As, P). *Physica B* **177**, 123–126 (1992).
40. Ohta, S., Kaneko, T., Yoshida, H., Kanomata, T. & Yamauchi, H. Pressure effect on the magnetic transition temperatures and thermal expansion in chromium ternary pnictides CrMAs (M = Ni, Rh). *J. Mag. Mag. Mater.* **150**, 157–164 (1995).
41. Jain, A. et al. Commentary: The Materials Project: a materials genome approach to accelerating materials innovation. *APL Mater.* **1**, 011002 (2013).
42. Kresse, G. & Furthmüller, J. Efficient iterative schemes for ab initio total-energy calculations using a plane-wave basis set. *Phys. Rev. B* **54**, 11169–11186 (1996).
43. Kresse, G. & Furthmüller, J. Efficiency of ab-initio total energy calculations for metals and semiconductors using a plane-wave basis set. *Comput. Mater. Sci.* **6**, 15–50 (1996).
44. Kresse, G. & Hafner, J. Ab initio molecular dynamics for liquid metals. *Phys. Rev. B* **47**, 558–561 (1993).
45. Koepnick, K. & Eschrig, H. Full-potential nonorthogonal local-orbital minimum-basis band-structure scheme. *Phys. Rev. B* **59**, 1743–1757 (1999).
46. Perdew, J. P., Burke, K. & Ernzerhof, M. Generalized gradient approximation made simple. *Phys. Rev. Lett.* **77**, 3865–3868 (1996).
47. Deyris, B. et al. Influence de l'électronégativité sur l'apparition de l'ordre dans les phases $MM'As$ (M=Ru, Rh, Pd; M' = element des transition 3d). *Ann. Chim.* **4**, 411–417 (1979).
48. Sandratskii, L. M. Symmetry analysis of electronic states for crystals with spiral magnetic order. I. General properties. *J. Phys.: Condens. Matter* **3**, 8565–8585 (1991).
49. Kresse, G. & Joubert, D. From ultrasoft pseudopotentials to the projector augmented-wave method. *Phys. Rev. B* **59**, 1758–1775 (1999).
50. Blöchl, P. E. Projector augmented-wave method. *Phys. Rev. B* **50**, 17953–17979 (1994).
51. Lejaeghere, K., Bihlmayer, G. & Björkman, T. et al. Reproducibility in density functional theory calculations of solids. *Science* **351**, aad3000 (2016).
52. Momma, K. & Izumi, F. VESTA3 for three-dimensional visualization of crystal, volumetric and morphology data. *J. Appl. Crystallogr.* **44**, 1272–1276 (2011).

ACKNOWLEDGEMENTS

Y.N.H. is supported by the National Natural Science Foundation of China (under Grant No. 11904319), and she thanks Bao Weicheng for valuable help in this research. I.I.M. acknowledges support from the U.S. Department of Energy through the grant No. DE-SC0021089.

AUTHOR CONTRIBUTIONS

I.I.M. initiated and supervised the project. All authors conducted the research. Y.N.H. and I.I.M. developed the spiral calculations. Y.N.H. performed the fitting analysis. H.O.J. performed the electronic structure calculations. I.I.M. provided theoretical support. All authors contributed to the data analysis and to writing of the paper.

COMPETING INTERESTS

The authors declare no competing interests.

ADDITIONAL INFORMATION

Supplementary information The online version contains supplementary material available at <https://doi.org/10.1038/s41535-023-00562-x>.

Correspondence and requests for materials should be addressed to Igor I. Mazin.

Reprints and permission information is available at <http://www.nature.com/reprints>

Publisher's note Springer Nature remains neutral with regard to jurisdictional claims in published maps and institutional affiliations.



Open Access This article is licensed under a Creative Commons Attribution 4.0 International License, which permits use, sharing, adaptation, distribution and reproduction in any medium or format, as long as you give appropriate credit to the original author(s) and the source, provide a link to the Creative Commons license, and indicate if changes were made. The images or other third party material in this article are included in the article's Creative Commons license, unless indicated otherwise in a credit line to the material. If material is not included in the article's Creative Commons license and your intended use is not permitted by statutory regulation or exceeds the permitted use, you will need to obtain permission directly from the copyright holder. To view a copy of this license, visit <http://creativecommons.org/licenses/by/4.0/>.

© The Author(s) 2023